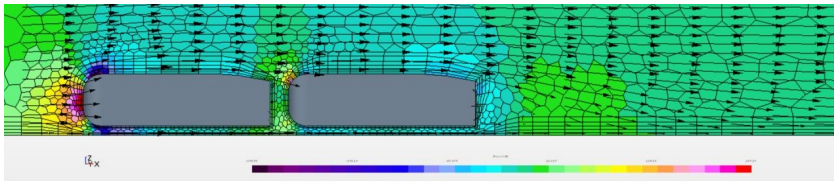

(a) Mesh of 1.0 m base size

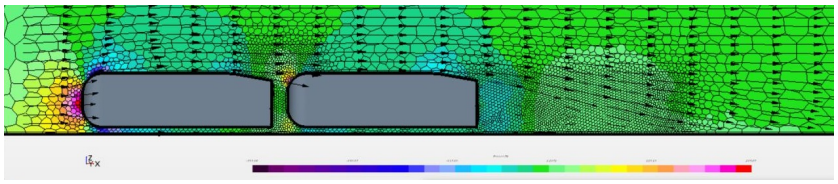

(b) Mesh of 0.15 m base size

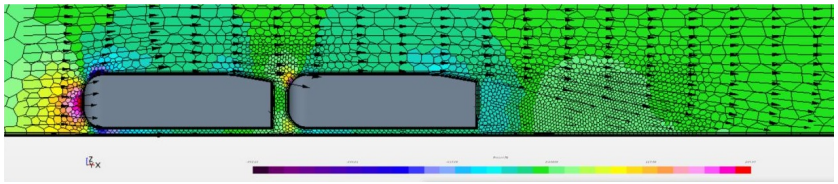

(c) Mesh of 0.22 m base size

Figure 3.2: Comparison of meshes for double Ahmed body set-up

3.2.2 Adjoint flow solution

Adjoint models calculate gradient values of quantities of interest from a initial (or primal) converged flow solution. From hence, the sensitivity of some model output (in this case, drag) to multiple model inputs (geometry at every point in the mesh) can be determined [5]. Since each adjoint equation is derived from one of the primal flow equations, this computation can be accomplished within about the same order of magnitude of time as the primal solution. This makes the adjoint approach significantly faster for free-form shape optimization than parametric methods, where execution time increases exponentially with the number of parameters, which must be large to provide for flexibility in altering the geometry.

However, adjoint solvers are not without their own drawbacks. The convergence of the adjoint solution depends heavily upon the quality of the primal solution, and as such tweaks must be made to allow the primal solution to converge further than usual, which often come at the cost of accuracy. Furthermore, different software packages introduce additional restrictions on their adjoint solver implementations, as they might not yet support some features. For instance, flows might be limited to the steady, incompressible

regime, and not all turbulence models might be supported.

The adjoint also requires the use of the coupled solver. In STAR-CCM+, this resulted in a loss of convergence quality, as the coupled solver struggled to lower the residuals past 1×10^{-3}. My supervisor advised changing to a first-order discretization from a second-order one, which significantly improved convergence at the slight expense of a loss of real-world accuracy. Additionally, the turbulence model was changed from $k - \varepsilon$ to the simpler Spalart-Allmaras, which not only improved convergence but also allowed for unfreezing turbulence within the adjoint solution. All told, these measures allowed convergence of residuals to around 1×10^{-7}, the bare minimum typically needed for a successful adjoint solution.

3.2.3 Shape optimization

In STAR-CCM+, the officially supported workflow for shape optimization is iterative. The shape sensitivity of the cost function(s) is computed from the converged adjoint solution, and used to morph the mesh as desired. From there, a new primal solution, adjoint solution, and shape sensitivity field are obtained, and the process repeated. By morphing in small increments, a smooth descent towards the local minimum may be achieved.

To understand the smoothness of the descent for this set-up, a fairly conservative scaling factor of 0.05 (i.e. the maximum displacement in each iteration will not exceed 5 % of the total permitted displacement) was chosen and the optimization was iterated to beyond twice the total permitted displacement. This was achieved in 35 iterations.

From Figure 3.3, it can be seen that the response of drag to the surface deformation is almost linear for this case, where displacement is constrained to a relatively small boundary. As such, a higher scaling factor may be used subsequently to achieve similar results within fewer iterations through more aggressive descent along the cost function.

The optimized geometry for the forward flow is characterized by two protrusions in the upper left and upper right corners of the face, and a recessed region covering most of the rest of the face (Figures 3.4 and 3.5).

The diagrams of the flow in the original geometry exhibit two dominant characteristics. Flow coming off the top surface of the front Ahmed body is forced downwards by the flow above it into a horizontal vortex system which tapers off towards the sides (Figure 3.6). There, the flow from the top combines with flow from the side surface to form a vertically oriented counter-rotating vortex pair (Figure 3.7). It appears that the recess better accommodates the shape of the horizontal vortex, while the protrusions accommodate the vertical vortices. This reduces the pressure experienced by

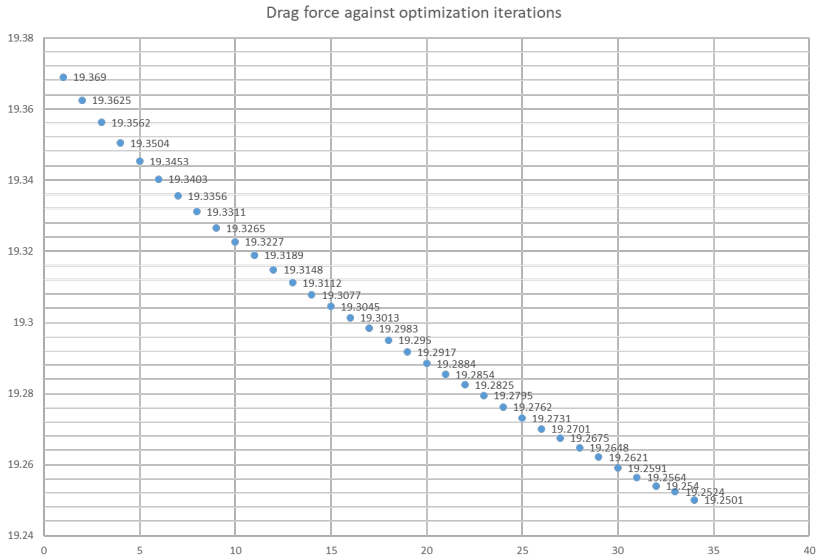

Figure 3.3: Drag force against optimization iterations

the rear Ahmed body, lowering drag thereby.

3.2.4 Reversed-flow adjoint solution and shape optimization

A similar process was undertaken for the reversed-flow set-up. The mesh study was not repeated; the meshing settings from the forward-flow case was reused, under the assumption that the flow phenomena of both cases would be similar enough that a mesh of the same fineness will be sufficient to resolve them.

The shape optimization workflow was then applied to the forward-flow and reversed-flow cases separately, using a scaling factor of 0.5. However, in the reversed-flow scenario, the primal solution diverged following the 4th iteration. A self-reinforcing instability occurred in the lower half of the target face, near the plane of symmetry, resulting in a highly deformed mesh with excessive skewness (see Figure 3.8).

To remedy this, the reversed-flow mesh was refined in the vicinity of the instability region (see Figure 3.9), with the hope that this would either resolve the instability, or allow the mesh to be more tolerant to extreme distortion. Additionally, the smoothing factor for the shape sensitivity field was increased from 0.05 to 0.1. Figure 3.10 demonstrates the effect of the smoothing factor. The forward-flow case was also rerun with the increased

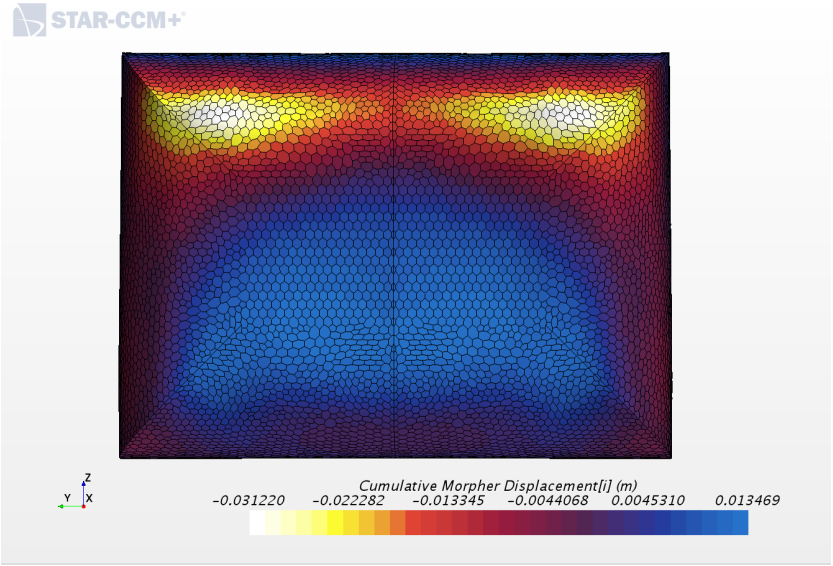

Figure 3.4: Frontal view of optimized face

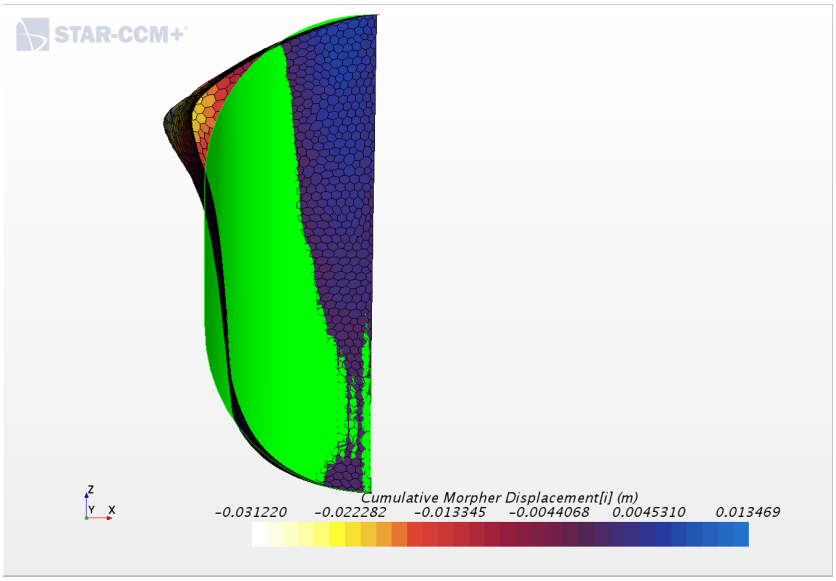

Figure 3.5: Side profile of optimized face, sectioned along symmetry plane. Original geometry shown in green.

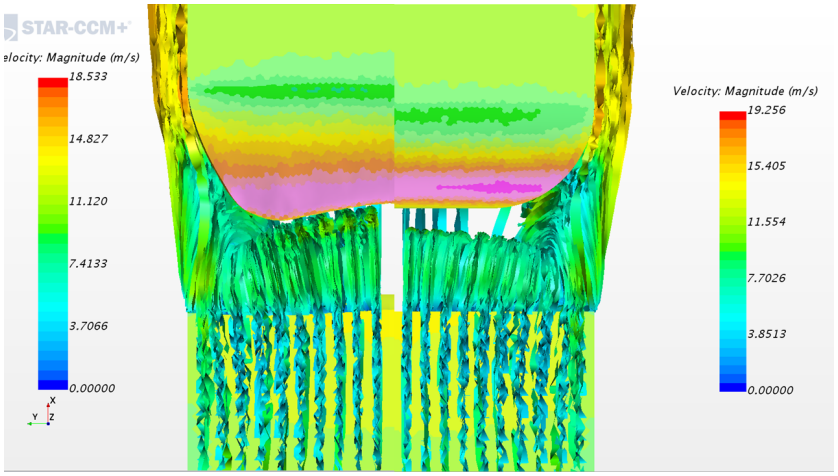

Figure 3.6: Side-by-side comparison of streamlines and pressure distribution on Ahmed body surface, top view. Original geometry shown on left, final geometry shown on right.

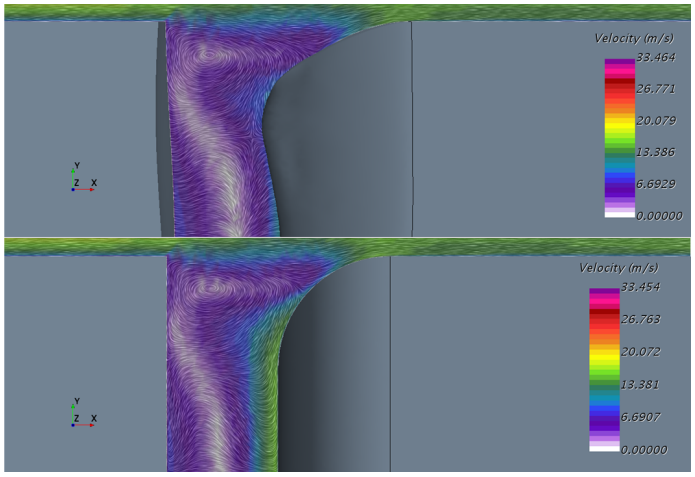

Figure 3.7: Comparison of velocity vector field along symmetry plane. Original geometry shown below, final geometry above.